ADVANCED MATERIALS
www.advmat.de

Piezoelectric Fibers for Conformal Acoustics

*Noémie Chocat, Guillaume Lestoquoy, Zheng Wang, Daniel M. Rodgers, John D. Joannopoulos, and Yoel Fink**

The first modern ultrasound transducer was developed after the tragedy of the Titanic in 1912, when the need arose for an echolocating device to detect icebergs and, later on, submarines. The success of sonar technology stimulated research in this field and led to the development of a large number of important applications such as non-destructive testing (NDT) and medical imaging, with an ever higher accuracy both in direction and range. In recent years, new uses of ultrasound transducers have emerged, particularly in - but not limited to - the medical field, such as photoacoustic imaging of the brain,[1] bone healing,[2] focused ultrasound surgery,[3] and ocean observation.[4] These applications ideally require large-area, flexible, and addressable transducer arrays, where the amplitude and phase of each individual device can be independently controlled. Several approaches have been pursued to address this challenge. A specially active area of research has been electroactive polymers, which have been widely investigated as an alternative to piezoceramics.[5] In particular, the large values of piezoelectric constants for poly(vinylidene fluoride) (PVDF) and copolymers such as poly(vinylidene fluoride trifluoroethylene) (P(VDF-TrFE)), coupled with their mechanical compliance and processability make them especially suited for large-area flexible applications. Furthermore, their large bandwidth and low acoustic impedance are an advantage for many medical uses. Another promising path involves capacitive micromachined ultrasonic transducers (CMUTs).[6] These approaches, however, leave some key challenges unresolved: device reliability issues due to charge trapping, constraints on the device area due to wafer-based processes, acoustic cross-talk, and complex electronic integration.[7]

N. Chocat, Prof. Y. Fink
Department of Materials Science and Engineering
Massachusetts Institute of Technology (MIT)
Cambridge, MA 02139, USA
E-mail: yoel@mit.edu
G. Lestoquoy, D. M. Rodgers[†]
Department of Electrical Engineering
and Computer Science
MIT, Cambridge, MA 02139, USA
Prof. Z. Wang,[+] Prof. J. D. Joannopoulos, Prof. Y. Fink
Research Laboratory of Electronics
MIT, Cambridge, MA 02139, USA
Prof. Z. Wang, Prof. J. D. Joannopoulos
Department of Physics
MIT, Cambridge, MA 02139, USA
[+] Present address: Department of Electrical and Computer Engineering, University of Texas at Austin, Austin, TX 78712, USA
[†] Present address: Orbital Sciences Corporation, 21839 Atlantic Blvd, Dulles, VA 20166, USA

DOI: 10.1002/adma.201201355

Recently developed multimaterial fibers present a number of attractive properties that can address these issues. The preform-based thermal drawing process offers a scalable means of producing kilometer-long fiber devices with submillimetric cross-sectional dimensions.[8] These long and flexible fibers can easily be assembled into large-scale conformal constructs, such as fabrics and sparse meshes.[9] Furthermore, monolithic integration of electrodes into the fiber enables straightforward electrical connection of the device to an external electrical circuit.[8] The latest advances in this field have led to the development of P(VDF-TrFE)-based piezoelectric fibers that are capable of acoustic emission and detection over a broad range of frequencies, from the tens of Hz to the tens of MHz.[10] While the small cross-sectional area of these fibers enables both miniaturization and flexibility, it seemingly involves an equally small *active* area that potentially limits the fiber performance. Here we introduce a new large-active-area fiber design that addresses a fundamental tradeoff between the requirement of maximizing the surface area of the acoustic device, and the inherent energy penalty associated with generating large area interfaces. This is achieved by confining the low viscosity crystalline ferroelectric medium between highly viscous boundaries, thus controlling the kinetics of the fiber thermal drawing process. We perform interference experiments to show that this novel device is coherent in the axial dimension, and we demonstrate how the coherence property combined with the mechanical flexibility enables acoustic wavefront shaping through precise control over the fiber curvature. Although the single fiber itself presents unique opportunities for minimally invasive sensing and imaging, in this work we take it one step further and analyze collective effects in multiple fibers. Coherent interferences and beam steering capabilities of multi-fiber phased arrays are demonstrated, thus establishing the possibility of assembling large-scale fiber constructs such as fabrics and meshes.

Piezoelectric transducers can be used both in emission and reception, depending on the application. When the transducer operates as a receiver, internal electrodes with a large surface area are desirable as they lead to a higher number of charges generated, and thus a better device sensitivity. As a transmitter, the fiber reaches maximal strain when the electric field is maximal, while remaining below the breakdown voltage. In these two regimes, the large-effective-area fiber design introduced in this paper enhances the transducer performance. Indeed, for a given cross-sectional area, a folded structure enables a several-fold increase in the electrode area and allows high electric fields without a high applied voltage since the piezoelectric layer is thinned down. This approach was developed for piezoceramic actuator stacks, and is of particular interest for use with our fabrication process. The fibers are produced by a thermal drawing technique from a macroscopic preform, which has the desired

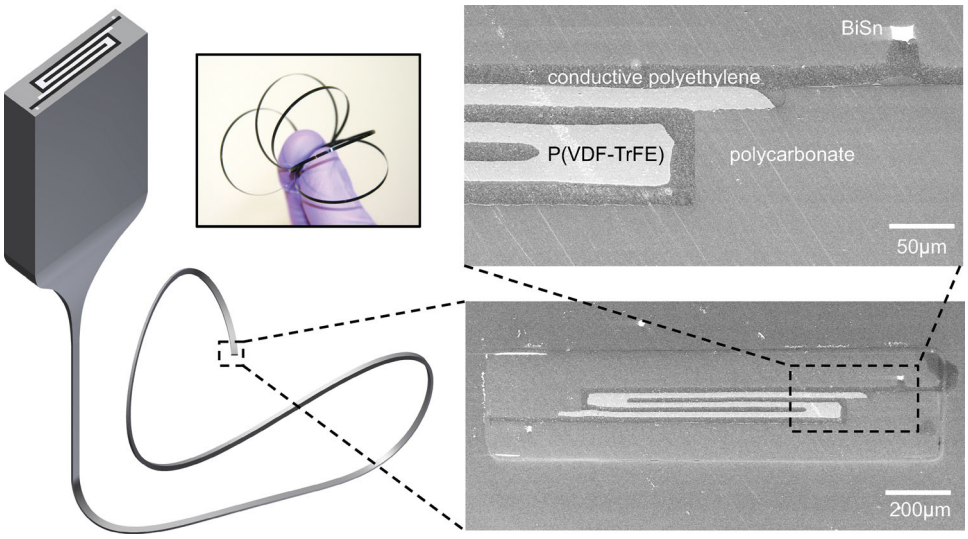

Figure 1. Schematic drawing of a preform drawn into a fiber along with SEM microscopy images of a piezoelectric fiber and magnification. Inset: Flexible piezoelectric-stack fiber.

device structure and geometry but is much larger in its cross-sectional dimensions (see Experimental). One of the appeals of this method is that the assembly of piezoelectric P(VDF-TrFE) layers and conductive polymer electrodes is done at the macroscopic level of the preform, which then yields tens of meters of fibers in a single draw. Therefore, the added cost and complexity of having multiple folded piezoelectric layers is minimal when compared to traditional layer-by-layer deposition techniques. Moreover, we expect the superior compliance and malleability of polymers over ceramics to reduce the risk of brittle failure and enable its use in tensile mode without preloading the device.[11]

As shown in **Figure 1**, the structure of the large-active-area piezoelectric fibers combines sharp corners and turns, numerous interfaces between materials, and large aspect-ratio geometries. Therefore, part of the challenge is to slow down the kinetics of surface energy driven phenomena during the draw, so as to prevent the fiber structure from evolving towards a more thermodynamically favorable geometry and to maintain a good structural integrity.[12] This is of particular importance here because the piezoelectric performance of ferroelectric devices relies critically on the success of electric poling and consequently the uniformity in the thickness of the ferroelectric layers. Typically, a strong electric field (>60 $MV.m^{-1}$), applied across the ferroelectric P(VDF-TrFE) layer through the internal electrodes, is required to permanently align the electric dipoles and achieve macroscopic polarization.[13] Given that the threshold of poling is close to the dielectric strength,[14] fluctuations in the ferroelectric layer thickness will reduce the average poling fields, because the applied poling voltage is limited by the thinnest portions where the onset of dielectric break-down begins. Thicker portions experience incomplete poling which leads to an overall sub-optimal piezoelectric response, an effect further aggravated by the nonlinear relation between the remnant polarization and the external electric fields.[15]

To address these issues, the fiber materials were carefully selected to meet precise thermo-mechanical and electrical criteria. Previous work has shown that P(VDF-TrFE) is particularly suited to the fiber fabrication process because it solidifies spontaneously from the melt in the ferroelectric β phase.[10] However, being a semi-crystalline polymer, P(VDF-TrFE) is drawn in a low-viscosity molten state and is particularly susceptible to capillary break-up. Therefore one of the key challenges was to identify an electrode material that would have a high viscosity (between 10^4–10^7 Poise) at the draw temperature, enabling it to be co-drawn with P(VDF-TrFE) in a high aspect-ratio geometry while resisting capillary break-up. Carbon-loaded polymers are good candidates for this role, although if their viscosity during the draw is too high, the carbon-black aggregates can undergo a high degree of breakdown resulting in a much-reduced conductivity.[16] Carbon-loaded polyethylene (CPE) was found to have a viscosity that is low enough to maintain a conductivity that is independent of the draw conditions, specifically the level of stress experienced by the fiber, while being high enough to avert capillary break-up (see Supplementary Information).

In order to gain more insight on the performance and limitations of individual fibers, in particular those associated with the new fiber geometry, we characterized their acoustic emission and electrical impedance, and compared the measurement with results from simulations. The acoustic characterization was performed in water, with a commercial piezoceramic transducer and the fiber transducers in immersion. A large water-tank (43 cm × 33 cm × 38 cm) and time-gated signal processing were employed to minimize the interferences both from acoustic reflections on the walls of the water tank and electromagnetic coupling between the fiber and the transducer. To measure the angular emission pattern of a single fiber, we fixed the distance between the fiber and the ceramic transducer, and rotated the fiber sample a few degrees along its long axis between each measurement. **Figure 2**a shows the acoustic radiation pattern of the fiber transducer at 900 kHz. The observed anisotropic

Adv. Mater. **2012**,
DOI: 10.1002/adma.201201355

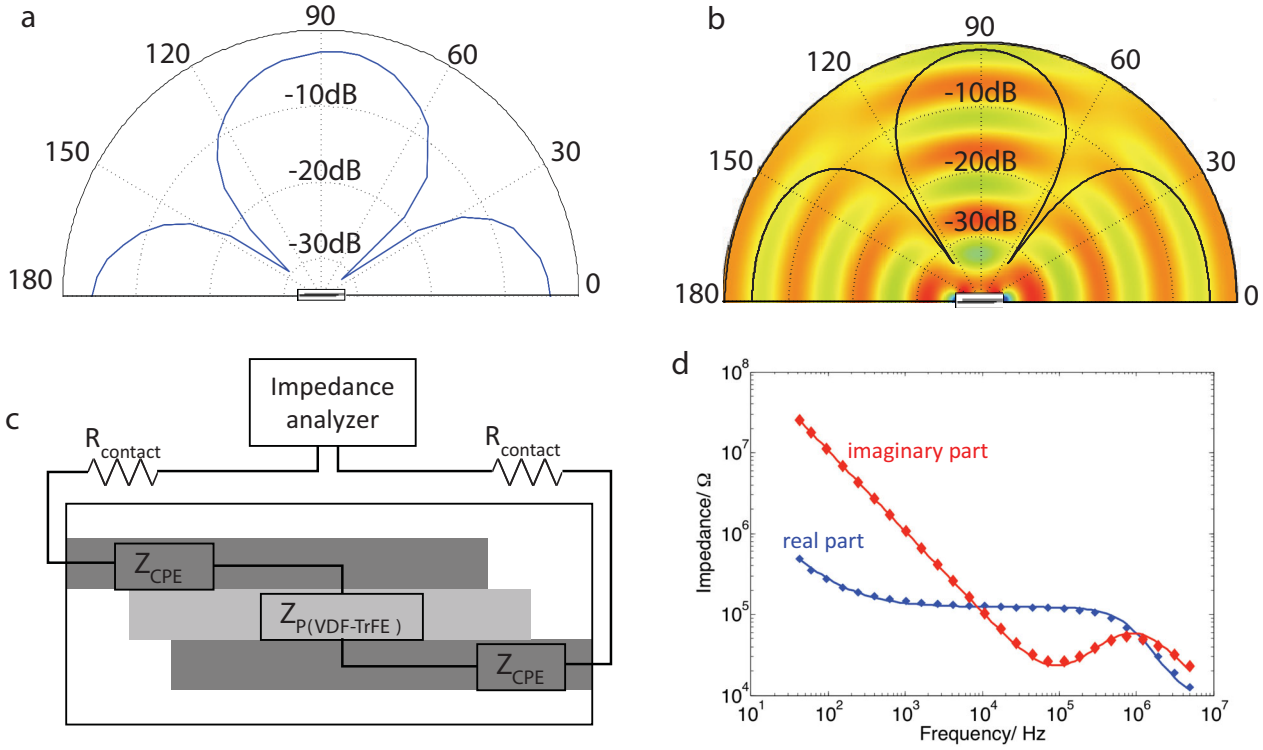

Figure 2. Acoustic piezoelectric fiber. a) Acoustic radiation pattern of the piezoelectric fiber measured in water at 900 kHz. b) Simulation of the far-field acoustic radiation pattern of a piezoelectric fiber in water at 900 kHz. c) Equivalent circuit model of a piezoelectric fiber connected to an impedance analyzer. d) Measured (diamonds) and simulated (solid line) electrical impedance real and imaginary parts.

angular emission along four axes displays a good fit with the simulations (Figure 2b). This clover-like pattern depends on the ratio of the outer dimensions to the acoustic wavelength, and on the design of the fiber transducer. Note how the angular widths of the lobes are inversely related to the length of the corresponding edge: the emission's directivity could thus be controlled by changing the fiber geometry.

Another important property of a piezoelectric fiber is its electrical impedance at various frequencies: not only is its knowledge required when designing interface circuits to deliver optimal power-efficiency and sensitivity, but it is also useful in determining the upper limit for the operational frequency, beyond which the transducer sensitivity rolls off rapidly.[10] We use an impedance analyzer to measure the frequency response of this impedance from 42 Hz to 5 MHz. Figure 2c displays the equivalent circuit of a fiber under test connected to the impedance analyzer. In this simplified approach, the different parts of the fiber along the path of the current are connected in series and characterized by their electrical impedance: Z_{CPE} for the conductive electrodes, $Z_{P(VDF\text{-}TrFE)}$ for the piezoelectric layer and a purely resistive term $R_{contact}$ to take into account losses at the connection with the setup. It has been reported that the otherwise constant resistivity of CPE decreases at frequencies f above a critical frequency f_0 whose value highly depends on the polymer preparation.[17] We have repeatedly witnessed this effect in these fibers- with f_0 in the 0.5–10 MHz range - and have included it by considering the following frequency dependence of $Z_{CPE}(f)$:

$$Z_{CPE}(f) = \frac{R_{CPE}}{1 + j\frac{f}{f_0}} \quad (1)$$

where R_{CPE} is the low frequency resistance of the electrode. The impedance of the P(VDF-TrFE) layer is calculated as that of a parallel plate capacitor, so that:

$$Z_{P(VDF-TrFE)}(f) = \frac{1}{j\frac{\varepsilon_p S_p}{t_p} 2\pi f} \text{ with } \varepsilon_p = \varepsilon_p' + j\varepsilon_p'' \quad (2)$$

where S_p, t_p and ε_p are resp. the surface of ferroelectric polymer in contact with the electrodes, its thickness and its dielectric permittivity. ε_p has a real and imaginary part that are both considered as frequency independent in our approach. The overall impedance of the system is thus modeled as a function of the driving frequency f by adding its components:

$$Z_0(f) = 2R_{contact} + 2Z_{CPE}(f) + Z_{P(VDF-TrFE)}(f) \quad (3)$$

Figure 2d displays the real and imaginary parts (resp. blue and red dots) of the measured impedance spectrum for a 3-cm long piezoelectric fiber. Fitting the model derived from the equivalent circuit to these measurements leads to a set of retrieved values [$R_{contact}$ = 4 kΩ, R_{CPE} = 58 kΩ,

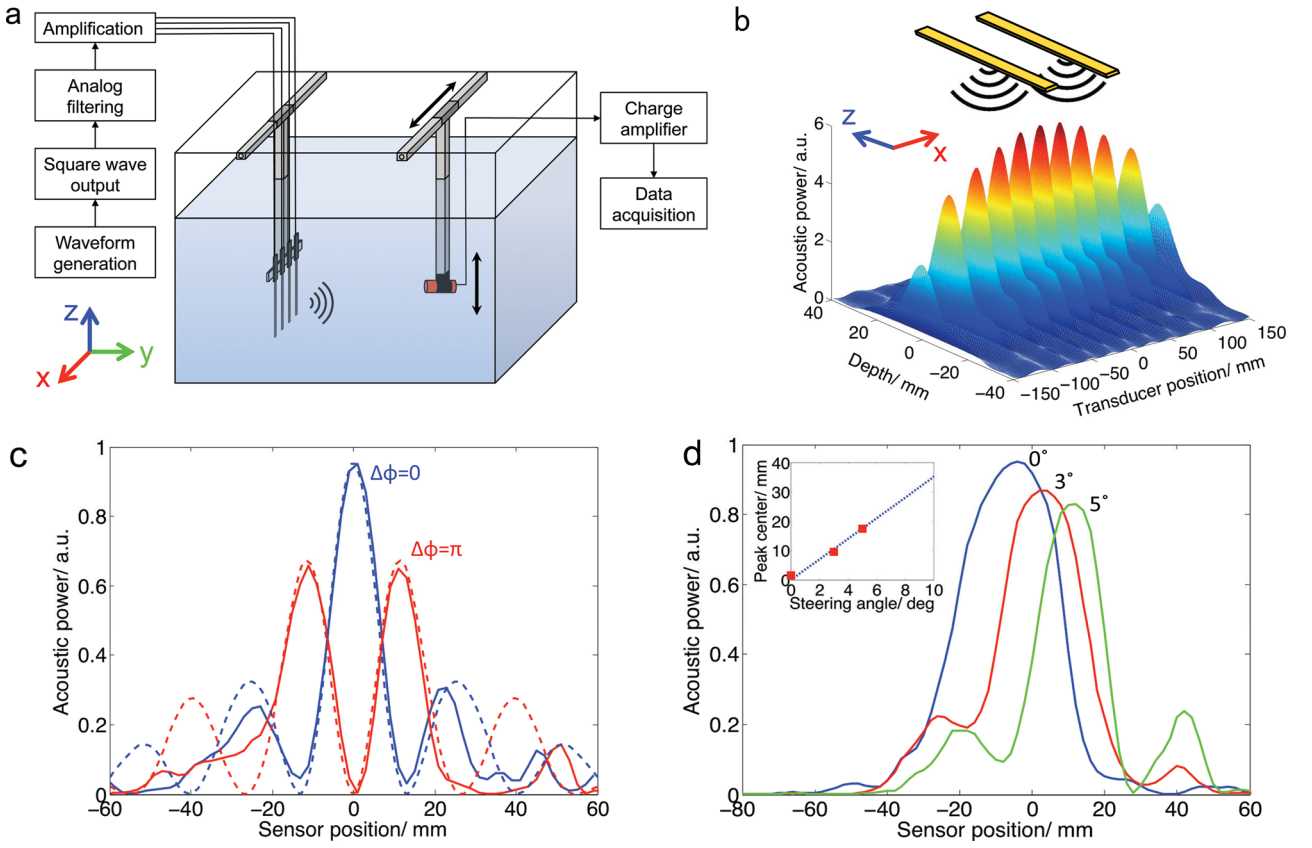

Figure 3. Piezoelectric fiber arrays. a) Schematic of under-water acoustic characterization set-up. b) 3D representation of the acoustic pressure field of a two fiber array emitting in phase. c) Two fiber array: measured (solid line) and simulated (dotted line) acoustic power along x at a distance of y = 20 mm from the array. d) Four fiber array: measured acoustic power along x at a distance of y = 20 mm from the array. Inset: main peak position as a function of the steering angle from the measurements (rectangles) and the theory (dotted line).

f_0 = 890 kHz, $\varepsilon'_p = 8.4\ \varepsilon_0$, $\varepsilon''_p = -0.12\ \varepsilon_0$] for which the theoretical $Re(Z_0(f))$ and $Im(Z_0(f))$ (solid lines in Figure 2d) closely match the experimental data. Furthermore, the values to which our model leads for ε'_p and ε''_p are consistent with the literature.[18] When connected to a controlling circuit such as the one used in the following section, the fiber can therefore be replaced by its equivalent circuit for all predicting purposes regarding its electrical behavior in this broad range of frequencies.

One of the interesting features of fiber transducers is that they can be assembled in dense arrays and woven into conformal fabrics. To illustrate this possibility, phased arrays of two and four piezoelectric fibers were constructed, and beam steering measurements were performed in water. **Figure 3**a shows the measurement setup in which fibers held parallel along a vertical (Z) axis and facing the same (Y) direction are driven at 600 kHz with an adjustable phase difference between consecutive fibers. This frequency was selected because it lays in the overlapping region of the operational bandwidths of the commercial transducer and the analog chips used in the measurement (see Experimental). The acoustic power pattern in the XZ plane is then measured with a commercial transducer at a fixed distance of 20 cm from the fibers. Figure 3b shows a simulated 2D map of the acoustic power generated by the interference between two piezoelectric fibers driven in phase. This pattern is numerically calculated but can be analytically described for small x and z by the following diffraction equation:[19]

$$P \propto sinc^2\left(\frac{\pi w x}{\lambda y}\right) sinc^2\left(\frac{\pi L z}{\lambda y}\right)\left(1 + cos\left(\frac{2\pi}{\lambda}\frac{dx}{y}\right)\right) \quad (4)$$

where the width w and the length L of the fiber determine the slowly varying envelope of the radiation pattern in the X and Z directions respectively. The extended length of the fiber transducers (40 mm for the tested device) results in a rapid decay of the acoustic power along Z, and a radiation pattern that is focused around the X-axis. Figure 3c compares the measurements with the theory for this two-fiber array in the cases where the fibers are in phase ($\Delta\phi = 0$) and out of phase ($\Delta\phi = \pi$). These interference patterns show that the two fibers emit in a coherent manner, a proof of the fiber device uniformity over extended lengths. The differences between theoretical and experimental results can be attributed to variations in emitting power and orientation from one fiber to the other.

The ability to control and focus acoustic energy is further improved by increasing the number of fibers being independently driven in the phased array. For example, with four fibers,

Adv. Mater. 2012,
DOI: 10.1002/adma.201201355

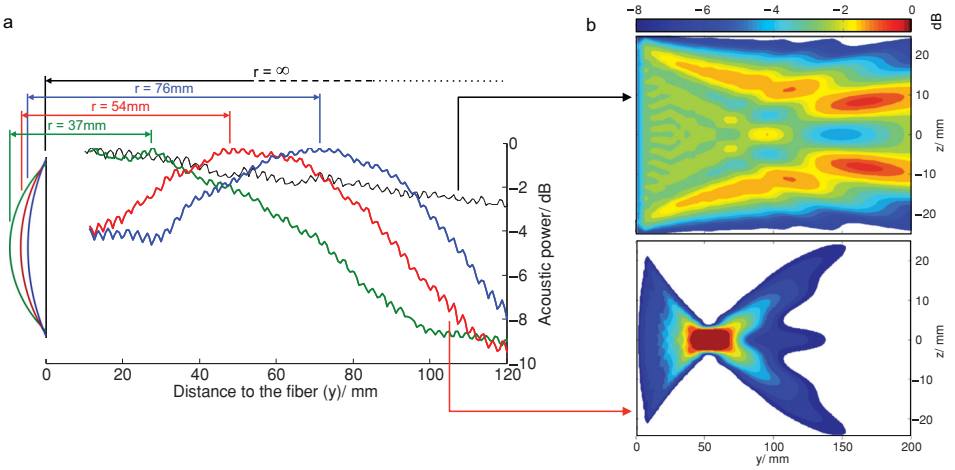

Figure 4. a) Measured acoustic power along the y-axis for different bending radii. b) Simulation of the acoustic pressure field in the x = 0 plane for a flat fiber (top) and for a fiber with bending radius equal to 54 mm (bottom).

one can perform beam steering by applying a relative phase difference

$$\Delta\phi = \frac{2\pi * f * d sin\theta}{c} \quad (5)$$

between adjacent fibers. Here f is the frequency, d the pitch (i.e. the distance between two consecutive fibers, along the X axis), c the speed of sound in water, and θ the desired steering angle. This measurement was carried out with steering angles from 0° to 5° (Figure 3d). The inset shows that there is a very good fit between the expected and measured positions of the central lobe.

By applying a parabolic phase difference between transducers along the multi-fiber array, one could also focus the acoustic beam.[19] However, the mechanical flexibility of the piezoelectric fibers permits an alternative approach to beam focusing using a *single* fiber. Indeed, by controlling the bending radius of a piezoelectric fiber, one can focus the acoustic beam at a designated distance from the fiber center. As presented in **Figure 4**, the emission profile of a bent fiber transducer differs radically from that of a straight fiber. Simulations done for 5-cm long fibers emitting at 600 kHz show that when the fiber is straight, the near-field region extends beyond 200 mm from the fiber. In contrast, with a bent fiber, the acoustic power is concentrated close to the fiber and is focused at a distance approximately equal to the bending radius. Measurements were performed using the same underwater set-up as shown in Figure 3a, but with the piezoceramic transducer traveling along the Y axis, that is, varying its distance to the emitting fiber. The results are shown in Figure 4b for bending radii ranging from 37 to 76 mm on a 5-cm long fiber, and compared to the emission profile of a straight fiber. These results demonstrate a clear effect of the fiber bending on the presence and location of the focal point, and illustrate the potential to construct flexible acoustic devices that have capabilities beyond those of their rigid counterparts.

In summary, we have demonstrated materials and structures that allow an enhancement of the performance of piezoelectric fibers through an increased effective area, and the associated large degree of freedom in controlling acoustic fields imparted by the mechanical flexibility. A new large-active-area structure was designed and fabricated and both acoustic and electrical characterization of this device was performed. As a proof-of-concept, two- and four-fiber phased arrays were assembled to show coherent interference and beam steering capabilities. Beam focusing through controlled bending of a single fiber gives a demonstration of the immense potential that lies in the ability of fibers to take arbitrary shapes. The combination of fiber tolerance to bending and twisting, anisotropic angular emission and possibility of assembly in multi-fiber phased arrays creates unprecedented opportunities in the design of large-area conformal acoustic devices. This work paves the way towards large-area, flexible and adjustable acoustic emission and sensing of complex, three-dimensional patterns for a variety of applications.

Experimental Section

Preform Preparation and Fiber Drawing: 300 µm-thick P(VDF-TrFE) films were prepared from 70:30 molar ratio pellets (Solvey) melt-pressed at 180 °C and 100 bars. They were assembled with 300 µm-thick CPE layers (Measurement Specialities) and metallic electrodes ($Bi_{58}Sn_{42}$ eutectic alloy, Indium Corporation) in a polycarbonate bar cladding (McMaster). The preform was consolidated under vacuum at 185 °C for ~20 minutes to remove trapped gas. This final preform was 38mm wide, 11 mm thick, and 200 mm long. It was then thermally drawn in a three-zone vertical tube furnace with the top-zone temperature at 150 °C, the middle-zone temperature at 230 °C, and the bottom-zone temperature at 110 °C. With this procedure, meters of fibers were drawn with thicknesses ranging from 230 to 370 µm (widths ranged from 800 µm to 1.3 mm).

Acoustic Measurements: all acoustic measurements were performed in water, using an Olympus immersion transducer V303-SU centered at 1 MHz and mounted on a linear motorized stage (Velmex Xslide with VXM stepping motor controller). For the radiation pattern characterization, a time-gate measurement algorithm was used to separate the acoustic signal from the electromagnetic interference, and to eliminate acoustic noise from reflections on the water-tank walls. The fiber device was mounted on a motorized rotational stage (Thorlabs CR1-Z7 with APT-dc servo controller). For the fiber array and flexed fiber measurements, a

continuous wave measurement was performed, using silicone foam absorbers along the water-tank walls to minimize reflections. Results shown in Figure 4 are obtained by averaging the raw measured acoustic power over one wavelength (2.4 mm at 600 kHz underwater) around the sensor position and normalizing. Both motorized stages were controlled using a LABVIEW interface.

Electrical Measurements: The electrical impedance characterization of the piezoelectric fibers was performed with a Hioki 3532-50 LCR HiTester impedance analyzer. Electrical contacts were made to the $Bi_{58}Sn_{42}$ electrodes by stripping away the polycarbonate cladding and attaching thin wires to the exposed electrodes with conductive silver paint.

Phased Array: The digital waveforms used to control the fiber transducers were generated in MATLAB and, using LABVIEW, were loaded into a Byte Paradigm GP 24–100 digital signal generator delivering a square wave which was then filtered by an analog chip in order to remove unwanted higher order harmonics, leaving only the desired fundamental frequency.[20] These filtered waveforms were then amplified and applied to the fiber transducers forming the array.

Simulations: Acoustic radiation pattern simulations were performed with the finite-element simulation package COMSOL Multiphysics (version 4.2), using the Acoustics module. All other simulations were done in MATLAB.

Supporting Information

Supporting Information is available from the Wiley Online Library or from the author.

Acknowledgements

This work was supported in part by the Materials Research Science and Engineering Center Program of the US National Science Foundation under award number DMR-0819762, and also in part by the US Army Research Office through the Institute for Soldier Nanotechnology at MIT under contract number W911NF-07-D-0004. We also thank the RLE for their support.

Received: April 3, 2012
Revised: June 1, 2012
Published online:

[1] J. Gamelin, A. Aguirre, A. Maurudis, F. Huang, D. Castillo, L. V. Wang, Q. Zhu, *J. Biomed. Opt.* **2008**, *13*, 024007.
[2] L. A. Cornejo, B. Jadidian, A. A. Winder, A. Safari, in *Proc. of the 11th IEEE Int. Symp. on Applications of Ferroelectrics*, *IEEE* **1998**, 259–263.
[3] G. T. Clement, J. White, K. Hynynen, *Phys. Med. Biol.* **2000**, *45*, 1071–1083.
[4] B. M. Howe, Yi Chao, P. Arabshahi, S. Roy, T. McGinnis, A. Gray, *IEEE J. Sel. Top. Appl.* **2010**, *3*, 507–521.
[5] E. Fukada, *IEEE T. Ultrason. Ferr.* **2000**, *47*, 1277–1290.
[6] O. Oralkan, A. S. Ergun, J. A. Johnson, M. Karaman, U. Demirci, K. Kaviani, T. H. Lee, B. T. Khuri-Yakub, *IEEE T. Ultrason. Ferr.* **2002**, *49*, 1596–1610.
[7] J. Chen, *J. Micromech. Microeng.* **2010**, *20*, 023001.
[8] A. F. Abouraddy, M. Bayindir, G. Benoit, S. D. Hart, K. Kuriki, N. Orf, O. Shapira, F. Sorin, B. Temelkuran, Y. Fink, *Nat. Mater.* **2007**, *6*, 336–347.
[9] A. Abouraddy, O. Shapira, M. Bayindir, J. Arnold, F. Sorin, D. Hinczewski, J. Joannopoulos, Y. Fink, *Nat. Mater.* **2006**, *5*, 532–536.
[10] S. Egusa, Z. Wang, N. Chocat, Z. M. Ruff, A. M. Stolyarov, D. Shemuly, F. Sorin, P. T. Rakich, J. D. Joannopoulos, Y. Fink, *Nat. Mater.* **2010**, *9*, 643–648.
[11] E. Flint, C. Liang, C. A. Rogers, in *Proc. of the 2nd Int. Conf. on Intelligent Materials*, CRC Press, Colonial Williamsburg, Virginia **1994**, 534–545.
[12] D. S. Deng, N. D. Orf, A. F. Abouraddy, A. M. Stolyarov, J. D. Joannopoulos, H. A. Stone, Y. Fink, *Nano Lett.* **2008**, *8*, 4265–4269.
[13] K. Kimura, H. Ohigashi, *Appl. Phys. Lett.* **1983**, *43*, 834–836.
[14] V. Giurgiutiu, S. E. Lyshevski, in *Micromechatronics: modeling, analysis, and design with MATLAB*, CRC Press, Taylor Francis Inc., Boca Raton, FL, United States **2009**.
[15] T. Furukawa, *Phase Transit.* **1989**, *18*, 143–211.
[16] N. C. Das, T. K. Chaki, D. Khastgir, *Polym. Int.* **2002**, *51*, 156–163.
[17] H. Kawamoto, in *Carbon Black–Polymer Composites, The Physics of Electrically Conducting Composites*, Marcel Dekker, New York **1982**.
[18] R. Gregorio, E. M. Ueno, *J. Mater. Sci.* **1999**, *34*, 4489–4500.
[19] A. Ghatak, in *Optics*, Tata McGraw-Hill Education, New Delhi, **2005**.
[20] D. M. Rodgers, *M.Eng. Thesis*, Massachusetts Institute of Technology, Cambridge, Massachusetts **2010**.